Soft particles assisted grain refinement and strengthening of an Al-Bi-Zn alloy subjected to ECAP

Hailong Jia [a], Ruben Bjørge [b], Knut Marthinsen [a], Ragnvald H. Mathiesen [c], Yanjun Li [a,*]

[a] Department of Materials Science and Engineering, Norwegian University of Science and Technology (NTNU), 7491 Trondheim, Norway

[b] SINTEF Materials and Chemistry, 7465 Trondheim, Norway

[c] Department of Physics, Norwegian University of Science and Technology, 7491 Trondheim, Norway

*Corresponding author at: Department of Materials Science and Engineering, Norwegian University of Science and Technology (NTNU), 7491 Trondheim, Norway.
E-mail address: yanjun.li@ntnu.no (Yanjun Li).

Abstract

With the aim to improve the strength of potential Pb-free Al-Bi based bearing alloys, an Al-6Bi-8Zn alloy was subjected to equal channel angular pressing (ECAP). To reveal the roles played by the soft Bi particles, an Al-8Zn alloy is compared. After five passes of ECAP (5P), ultrafine grained (UFG) microstructures are obtained in both alloys, while most of the Bi particles are deformed into the flake shapes. The yield strength (YS) of the as-deformed Al-6Bi-8Zn sample is more than three times as that of the as-cast sample. The influence of soft Bi particles on the deformation during ECAP and the final mechanical properties of the Al-6Bi-8Zn alloy are discussed. It is revealed that soft Bi particles have a strong influence on enhancing grain refinement during ECAP. At the same time, ECAP is found to accelerate the precipitation of the β(Zn) phase along grain boundaries (GBs).

Keywords: Aluminium alloy; ECAP; Soft particle; Precipitation; Tensile properties

1. Introduction

Aluminium-based hypermonotectic alloys (such as Al-Pb, Al-Bi and Al-In) are of particular interest as potential bearing materials due to the unique microstructures that form during solidification [1]. These alloys combine a volume fraction of soft secondary phase particles in a light weight α-Al matrix, resulting in a drastically low friction coefficient and very small wear resistance. Recently, the solidification of hypermonotectic alloys has gained increased interests again, because the European Union (EU) has proscribed the use of Pb containing alloys. Therefore, the developments of new Pb-free bearing materials are of great importance. In hypermonotectic Al-Bi (i.e. > 3.4 wt.% Bi) alloys, if a proper volume fraction of soft Bi particles homogeneously distribute within the Al matrix, they can resist high pulsating loads and give good overall tribological properties [2]. Also, weight saving is another special advantage of Al-based

bearing materials. So far, most of the research work has been focused on understanding the solidification behaviour of Al-Bi alloys and improving the distribution of Bi particles by different methods [3-7]. For example, Silva et al. studied the microstructural development [5, 7] as well as thermal parameters [6] during transient directional solidification of Al-Bi alloys. However, limited attention has been paid to improve the strength of Al-Bi alloys. Recently, Zha et al. [8] investigated the deformation behaviour of an Al-8Bi alloy subjected to equal channel angular pressing (ECAP), by which significant grain refinement could be achieved. However, the strength of the binary Al-Bi alloy processed by ECAP is still low [9].

With the aim to improve the strength of Al-Bi based alloys, a ternary Al-6Bi-8Zn alloy was subjected to ECAP in this work. One of the main reasons for adding Zn is that it can provide solid solution strengthening of the matrix without the need for additional heat treatment that could be detrimental to the Bi dispersion and distribution. On the other hand, it can improve the ductility of the severe plastic deformation (SPD) processed ultrafine grained (UFG) materials, for which plastic deformation localizes at the early stage of tensile deformation, resulting in early necking. It is well known that a high solute concentration of Cu and Mg in Al alloys can enhance ductility by improving the work hardening rate [10-13]. Recently, the pronounced beneficial effect of the Zn addition on improving tensile strength and ductility of nanostructured Al alloys has been reported [14, 15]. Firstly, this enhanced ductility is related to the enhanced work hardening that increases with increasing Zn content in the solid solution, resulting in an enhanced uniform elongation. Secondly, it is attributed to the formation of fine slip bands within the UFG Al-Zn alloys with a high Zn content and the uniform spreading of the fine slip bands all over the gauge length, which is found to be beneficial in the later stage of the tensile deformation, leading to the enhanced ductility of the Al-15Zn alloy [14]. In this study, a systematic study will be carried out to reach an in-depth understanding of the roles played by soft Bi particles on the deformation and grain refinement behaviours and their influence on the final mechanical properties of the Al-6Bi-8Zn alloy.

2. Experimental

The materials used in the present work were Al-8 wt.% Zn and Al-6 wt.% Bi-8 wt.% Zn alloys. These alloys were produced by melting commercial purity raw metals of Al, Zn and Bi in a clay-graphite crucible and then casted in a Cu mould (cooling rate ~3-15 K/s, dependent on distances to the mould wall). 0.5 wt.% Al-5Ti-1B master alloy was added into the melt before casting in order to get a fine equiaxed grain

structure. The as-cast ingots were machined into bars with dimensions of 100 mm × 19.5 mm × 19.5 mm. Considering about the low melting temperature of Bi (~271.3 ˚C), solution heat treatment was not conducted on the bars. Before ECAP, the bars were coated with a thin layer of a graphite lubricant to lower the friction during ECAP. Then, these bars were processed by ECAP through a 90˚ die via route Bc (rotated by 90˚ in the same sense between each pass) at RT, which leads to an imposed equivalent strain of about 1.0 per pass [16]. The samples were processed for various numbers of passes through the die, up to a maximum of five. A sample that was pressed by X passes of ECAP is labeled as XP.

Samples for microstructure observation, hardness and tensile test measurements were cut from the uniformly deformed regions of the ECAP processed bars in the longitudinal section. The deformed structures were characterized by backscattered electron (BSE) imaging, electron backscatter diffraction (EBSD) and transmission electron microscopy (TEM). Prior to EBSD examination, the sample surfaces were ion-milled at 3.5 V for 45 min (at a tilt angle of ~70˚, and with a gas flow rate of ~0.08 ml/min) using a Hitachi IM 3000 ion milling machine. EBSD was performed using a Hitachi SU-6600 field emission gun SEM (FEG-SEM) equipped with a Nordif EBSD detector and the TSL-OIM software. Vickers hardness measurements were conducted using a DKV-1S Vickers hardness testing machine under a load of 1 kg with a loading time of 15 s. The hardness values obtained were averaged from at least six separate measurements. The gauge length and thickness of the tensile specimens were ~5 mm and ~2 mm, respectively. Tensile tests were performed at a strain rate of 5×10^{-4} s^{-1} at RT by using a MTS 810 hydraulic universal testing machine with a 100 kN capacity.

3. Results and discussion

3.1. Initial microstructures before ECAP

As shown in Fig. 1, both the as-cast Al-6Bi-8Zn and Al-8Zn samples exhibit equiaxed α-Al grain structures with an average grain size of ~50 μm. In Fig. 1(a) and (b), the white spots are Bi particles, most of which are located along grain boundaries (GBs). Also, a small fraction of Bi particles are located inside grains of the matrix. The area fraction and the average size (area equivalent diameter) of Bi particles were measured to be ~1.2% and ~5 μm, respectively. It should be noted that the solidification structure is quite different from that in Ref. [8] where the grain size of the matrix is much larger and the Bi particles mostly

distributed along GBs as networks. From Fig. 1(d), it can be seen that there are no Zn precipitates in the as-cast Al-8Zn sample.

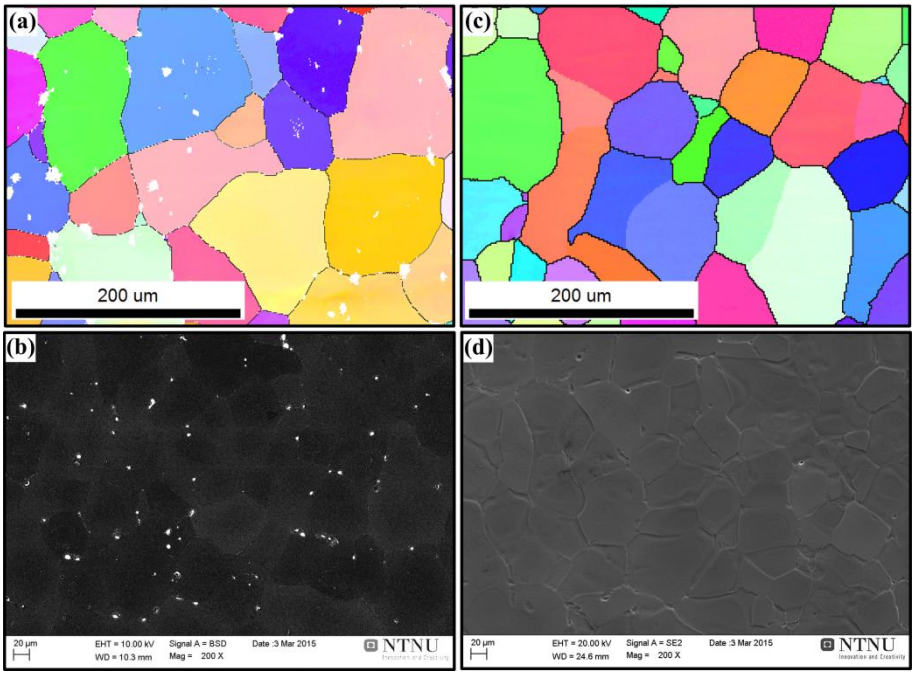

Fig. 1. (a) and (b) Microstructures of the as-cast Al-6Bi-8Zn alloy, and (c) and (d) microstructures of the as-cast Al-8Zn alloy. (a) and (c) are EBSD orientation imaging map (OIM), (b) and (d) are SEM-BSE micrograph.

3.2. Deformation microstructures after ECAP

Representative BSE images of the as-deformed Al-6Bi-8Zn samples are shown in Fig. 2. In the 1P sample, Bi particles have experienced strong shear deformation and most of the coarse Bi particles have been deformed into elongated flake shapes, which can be clearly seen from Fig. 2(b). Compared to the 1P sample, it seems that the Bi particles are further deformed into thinner and longer flakes in the 3P and 5P samples (Figs. 2(c) and (d)).

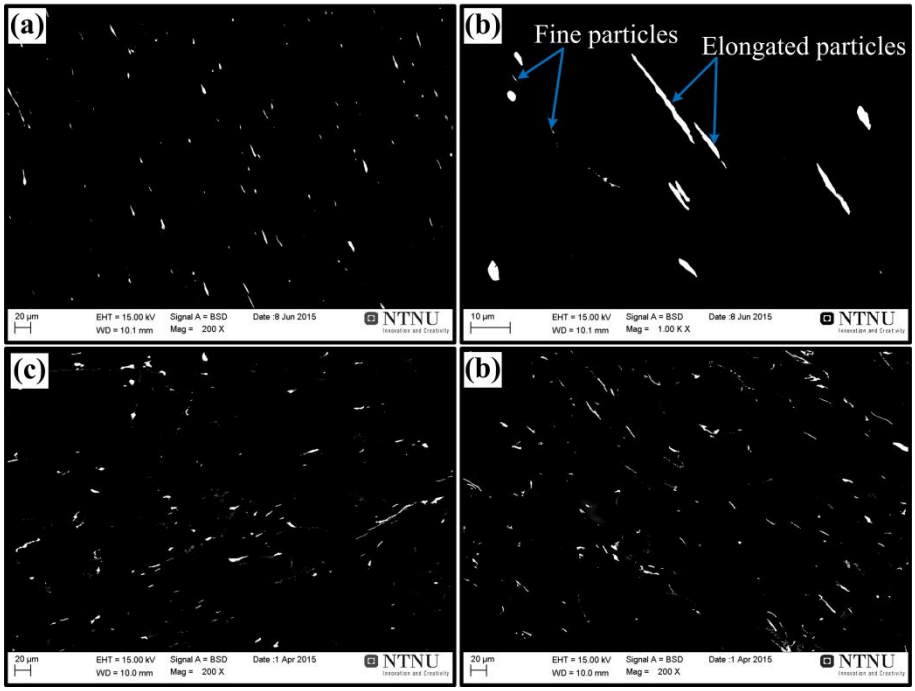

Fig. 2. BSE images of the as-deformed Al-6Bi-8Zn samples. (a) and (b) 1 pass, (c) 3 passes, and (d) 5 passes.

The deformation structure of the 1P Al-6Bi-8Zn sample revealed by EBSD is shown in Fig. 3. After one pass of ECAP (Fig. 3(a)), the coarse grains in the initial as-cast state have been deformed into elongated grains, mainly aligned at an angle of ~30˚ to the extrusion direction (ED). Fig. 3(b) is the magnified EBSD image of the area encircled by the rectangle in Fig. 3(a). Subgrains can be clearly observed inside some of the original grains, such as the grain GI. It seems that these subgrains are formed by the intersection of two sets of geometrically necessary boundaries (GNBs), some of which have evolved into HABs. For the majority of the coarse grains (e.g. the grains GII and GIII), only less well-defined subgrains have formed. The different deformation and grain refinement behavior of grains should be attributed to the difference in grain orientations, resulting in the structural heterogeneity. Additionally, as highlighted by the black ovals in Fig. 3(b), many fine grains have formed around Bi particles (the small black areas labelled by the black ovals) and at the original HABs. However, it seems that Bi particles locating at grain boundaries are more beneficial to grain refinement due to the more severe strain incompatibilities at GBs. From the boundary maps (Fig. 3(c) and (d)), it can be seen that a large quantity of LAB segments with misorientation of 2-15˚ have formed within the interiors of the original grains, and especially in the vicinity of HABs.

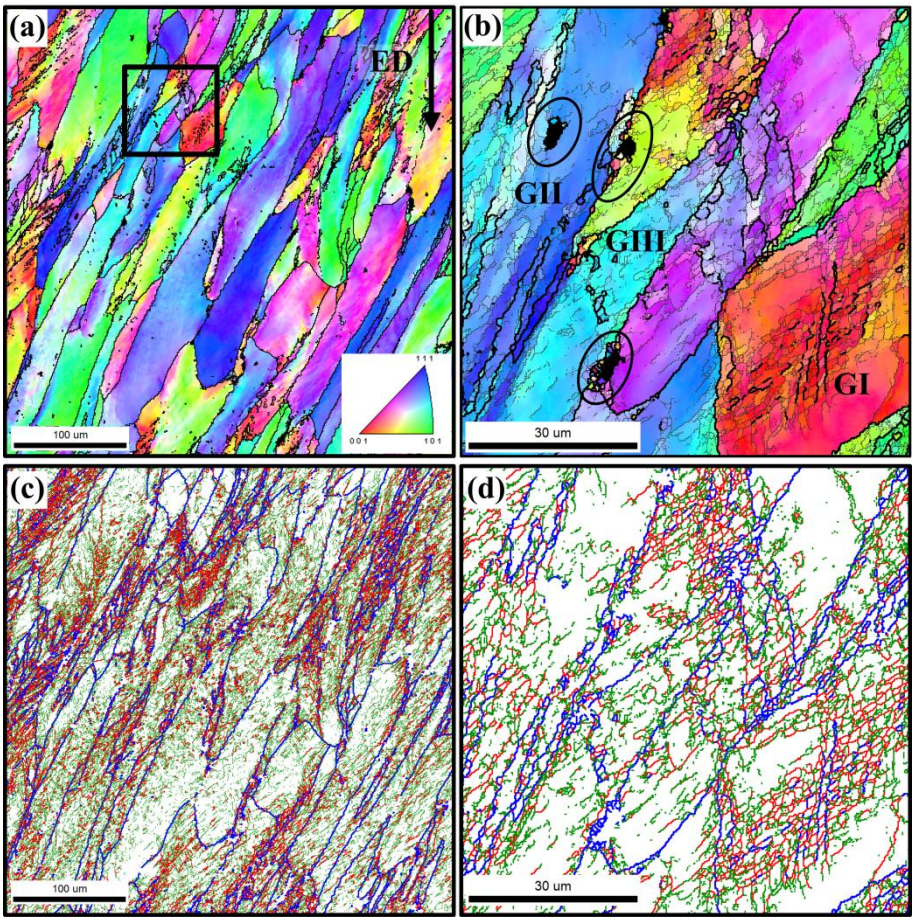

Fig. 3. EBSD results of the ECAP processed 1P Al-6Bi-8Zn sample. (a) and (b) Orientation maps, and (c) and (d) corresponding boundary maps of (a) and (b), respectively. (b) is a map with higher magnification of the area encircled by the rectangle in (a). In (a) and (b) black lines depict boundaries with misorientation angles of $15^\circ \leq \Theta < 180^\circ$, and thin grey lines in (b) depict boundaries with misorientation angles of $5^\circ \leq \Theta < 15^\circ$. The inset in (a) is the colour code for the orientation maps. In the boundary maps, green, red and blue lines depict boundaries with misorientation angles of $2^\circ \leq \Theta < 5^\circ$, $5^\circ \leq \Theta < 15^\circ$ and $15^\circ \leq \Theta < 180^\circ$, respectively.

Fig. 4(a) and (c) show the microstructure of the 5P Al-6Bi-8Zn sample. The coarse grains have been refined into equiaxed grains. For comparison, the grain structure of the 5P Al-8Zn sample is also given in Fig. 4(b) and (d). As can be seen, the grains of the 5P Al-6Bi-8Zn sample are significantly finer than that of the 5P Al-8Zn sample. As shown in Fig. 4(c) and (d), a large number of HAB segments connected with LAB segments can be observed. It indicates that the ultrafine equiaxed HAB grains have formed by continuous dynamic recrystallization (CDRX) via transformation of LABs into HABs.

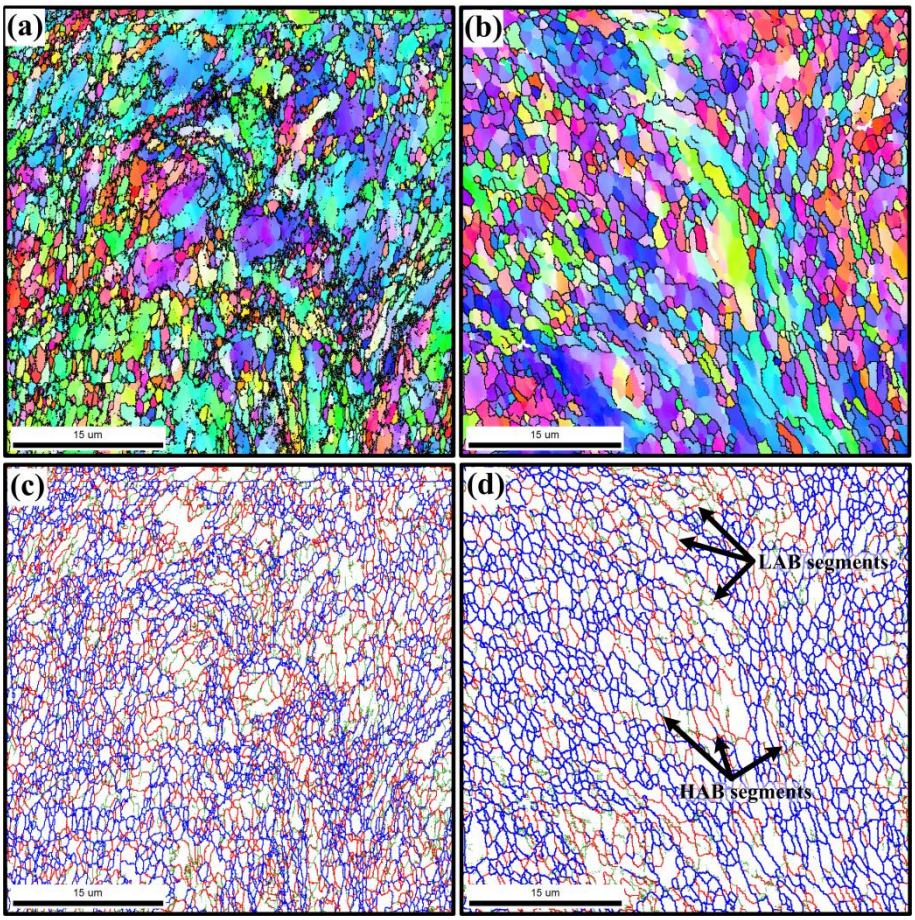

Fig. 4. EBSD results of the ECAP processed 5P Al-6Bi-8Zn and Al-8Zn samples. (a) and (c) Orientation and boundary maps of the 5P Al-6Bi-8Zn sample, respectively. (b) and (d) Orientation and boundary maps of the 5P Al-8Zn sample, respectively. In (a) and (b) black lines depict boundaries with misorientation angles of $15^\circ \leq \Theta < 180^\circ$. In boundary maps green, red and blue lines depict boundaries with misorientation angles of $2^\circ \leq \Theta < 5^\circ$, $5^\circ \leq \Theta < 15^\circ$ and $15^\circ \leq \Theta < 180^\circ$ respectively.

The measured average grain size evolution (with boundary misorientaions $\geq 5^\circ$), HAB fraction and the grain size distribution for the 5P Al-6Bi-8Zn samples in comparison with the 5P Al-8Zn sample are shown in Fig. 5. As can be seen from Fig. 5(a), the average grain size decreases considerably with increasing ECAP passes for both of these two alloys, especially during the first pass of ECAP. It is interesting to see that the average grain size of the 5P Al-6Bi-8Zn sample (~0.5 ± 0.1 μm) is significantly smaller than that of the 5P Al-8Zn sample (~0.9 ± 0.2 μm). Since Bi has nearly no solubility in Al solid solution, the only difference between the Al-8Zn alloy and the Al-6Bi-8Zn alloy is the existence of Bi particles in the Al matrix, thus, the different grain sizes in the 5P samples of these two alloys should be ascribed to the presence of the Bi particles. In other words, the presence of Bi particles has significantly

promoted the grain refinement of the Al matrix. This is due to the ease of forming ultrafine grains around the Bi particles as indicated in the 1P Al-6Bi-8Zn sample (Fig. 3(b)). In addition, the average grain size of the 5P Al-6Bi-8Zn sample is even smaller than that of the Al-10 wt.% Zn (~0.8 μm) processed by HPT after a shear strain of ~6 [17], which also confirms that the Bi particles play an important role in grain refinement during ECAP.

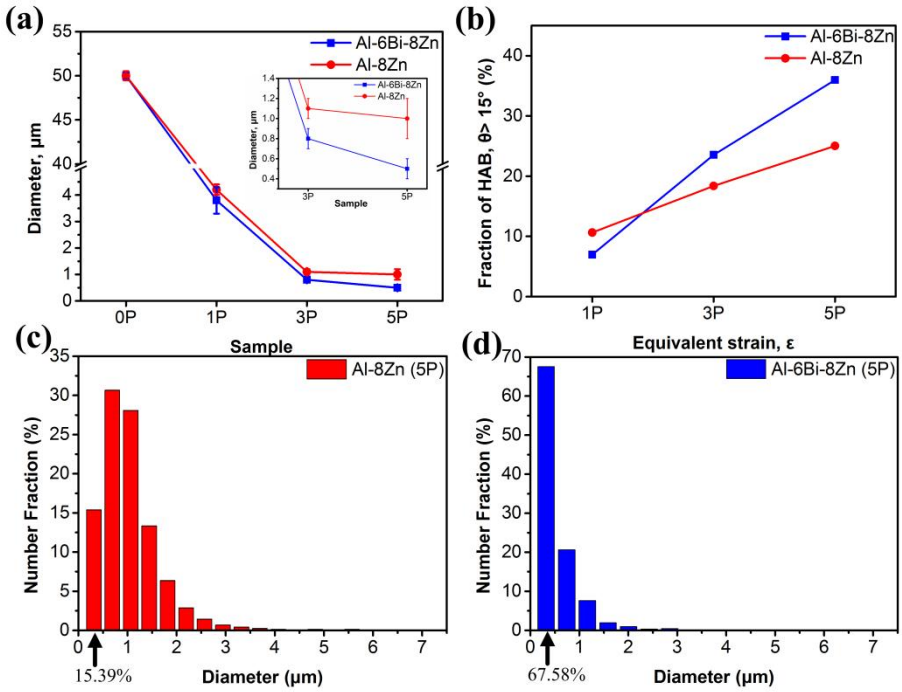

Fig. 5. (a) Evolution of the grain size (with boundary misorientations larger than 5˚) as a function of increasing number of ECAP passes; (b) HAB fraction evolution as a function of increasing number of ECAP passes; (c) and (d) grain size (with boundary misorientations larger than 5˚) distributions of the 5P Al-8Zn and 5P Al-6Bi-8Zn samples.

As shown in Fig. 5(b), after one pass of ECAP, although GBs are dominated by LABs, the HAB fraction of the 1P Al-8Zn sample is slightly higher than that of the 1P Al-6Bi-8Zn sample. It indicates the fast formation of LABs due to the soft Bi particles. With increasing deformation strain, the fraction of HAB increases in both alloys, implying that some LABs have evolved into HABs. This is in agreement with the EBSD micrographs. If comparing the increasing rate of HAB fraction with increasing ECAP passes, the Al-6Bi-8Zn alloy shows a faster increasing rate than the Al-8Zn alloy, resulting in a significantly higher fraction of HABs in the 5P Al-6Bi-8Zn alloy. It indicates that the development of HABs from LABs is more rapidly in the Al-6Bi-8Zn alloy. The influence of Bi particles on the grain boundary evolution can also be seen from the grain size distribution of the 5P samples. From Fig. 5(c) and

(d), we can see that the fractions of grains with diameter < 0.5 μm are ~68% for the 5P Al-6Bi-8Zn, while it is only ~15% for the Al-8Zn sample. The number fraction of ultrafine grains with diameter less than 0.5 μm in the 5P Al-6Bi-8Zn sample is almost 5 times that of the 5P Al-8Zn sample.

The impact of Bi particles on grain refinement during ECAP is further revealed by high resolution EBSD maps (step size 0.05 μm), which were taken in regions around coarse Bi particles subjected to both low (ε = 1) and high (ε = 5) strain deformations (see Fig. 6). In these maps, the actual misorientation angles of some boundaries in the vicinity of Bi particles are indicated (in degrees). After one pass of ECAP, the number density of subgrains adjacent to the Bi particle (the unindexed black area in Fig. 6) is much higher than that in areas far way from it. A large number of equiaxed subgrains with misorientation angles ~6-10˚ have formed and even some ultrafine HAB grains can be observed around the Bi particle. This is consistent with the HAB fraction evolution in Fig. 5(b), i.e., at reletively low strains, Bi particles contribute mainly to the generation of LABs. After five passes of ECAP, around each Bi particle, there is a large number of HAB grains with grain size < 0.5 μm. There is a trend that the grain size increases with increasing distance from the Bi particles. It can also be seen that the misorientations of HABs generally decrease with increasing distance from the Bi particle.

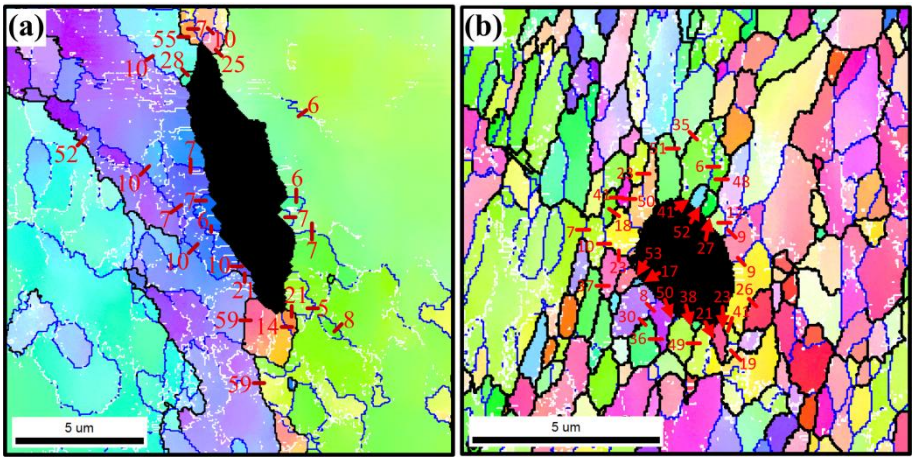

Fig. 6. High resolution (step size: 0.05 μm) EBSD maps of the as-deformed Al-6Bi-8Zn samples. (a) 1 pass, and (b) 5 passes. In the maps, orientation differences $\Delta\theta \geq 2^{\circ}$, $\Delta\theta \geq 5^{\circ}$ and $\Delta\theta \geq 15^{\circ}$ across boundaries are marked by white, blue and black lines, respectively. Misorientations of selected boundaries are given in degrees.

The easier development of ultrafine equiaxed grains around the Bi particles should be attributed to the different deformation behaviour between soft Bi particles and the relatively hard surrounding Al matrix.

This leads to a more severe deformation in the Al matrix in the vincity of Bi particles, which accelerates the formation of new LABs. With increasing deformation strain, the misorientation angles of LABs gradually increase, which evolve into HABs in consecutive deformation cycles. Therefore, Bi particles can promote the CDRX process. Here, the soft Bi particles in the Al-6Bi-8Zn alloy play a similar role as hard non-deformable particles in yielding strain incompatibilities during deformation. Coarse hard particles have been found to be effective in promoting grain refinement [18-24] during ECAP. However, metals and alloys containing hard particles are prone to cracking during ECAP due to particle breaking-up and void formation around particles, which limits the deformability at room temperature (RT) [25].

3.3. Precipitation of Zn particles

After five passes of ECAP, a large amount of nano-sized Zn particles can be observed in both of the alloys by TEM. Fig. 7 shows STEM (scanning transmission electron microscopy) images of the 5P Al-6Bi-8Zn and 5P Al-8Zn alloys, from which Zn particles (based on EDS results) can be seen and they are distributed mainly along GBs. The average size and number density of Zn particles are 80 nm and 5×10^{12} m^{-2} in the 5P Al-6Bi-8Zn alloy, which are larger than that of the 5P Al-8Zn alloy (the average size and number density of Zn particles are 40 nm and 3×10^{12} m^{-2}, respectively). This difference should be due to the higher fraction and average misorientation angles of the HABs in the Al-6Bi-8Zn sample. Different from the large Bi particles, nano-sized Zn particles can easily rotate with aluminium matrix during deformation, which cannot generate so much local deformation around the Zn particles. This is quite similar to the hard nano-sized particles. Also, as can be seen from Fig. 7(d), the TEM-SPED (scanning precession electron diffraction) study on the Zn precipitates in Al-Zn alloy showed that no LABs can be found around Zn particles, thus, it can be concluded that fine soft Zn particles in the Al-Zn and Al-Bi-Zn alloys cannot contributed to the grain refinement as the large Bi particles.

In this study, the content of Zn is 8 wt.%, which is much higher than the solubility of Zn in Al at RT (<1 wt.% [26]). Because of the fast cooling rate during casting, the matrices of these two as-cast alloys are supersaturated with Zn. However, as a result of ECAP, the supersaturated solid solution has a trend to decompose during deformation [14, 15] via dynamic precipitation, particularly as plastic work can raise the temperature during processing to ~50 ˚C [27]. The supersaturation is the driving force for precipitation, while the GBs provide the nucleation sites with low energy barriers. Compared to the non-deformed

samples, the as-deformed GBs are generally in a more disordered state [28], which would be expected to provide more effective nucleation sites than fully relaxed boundaries. The diffusion rate of Zn atoms during deformation is accelerated by the high vacancy and dislocation densities generated during ECAP, which provides short circuit diffusion paths. Furthermore, Zn atoms have a trend to segregate to dislocations. Since the rearrangement and self-organisation of dislocation substructure is a probable formation mechanism of the new GBs during ECAP, thus these newly formed GBs will be heavily enriched in Zn, contributing to the formation of Zn precipitates.

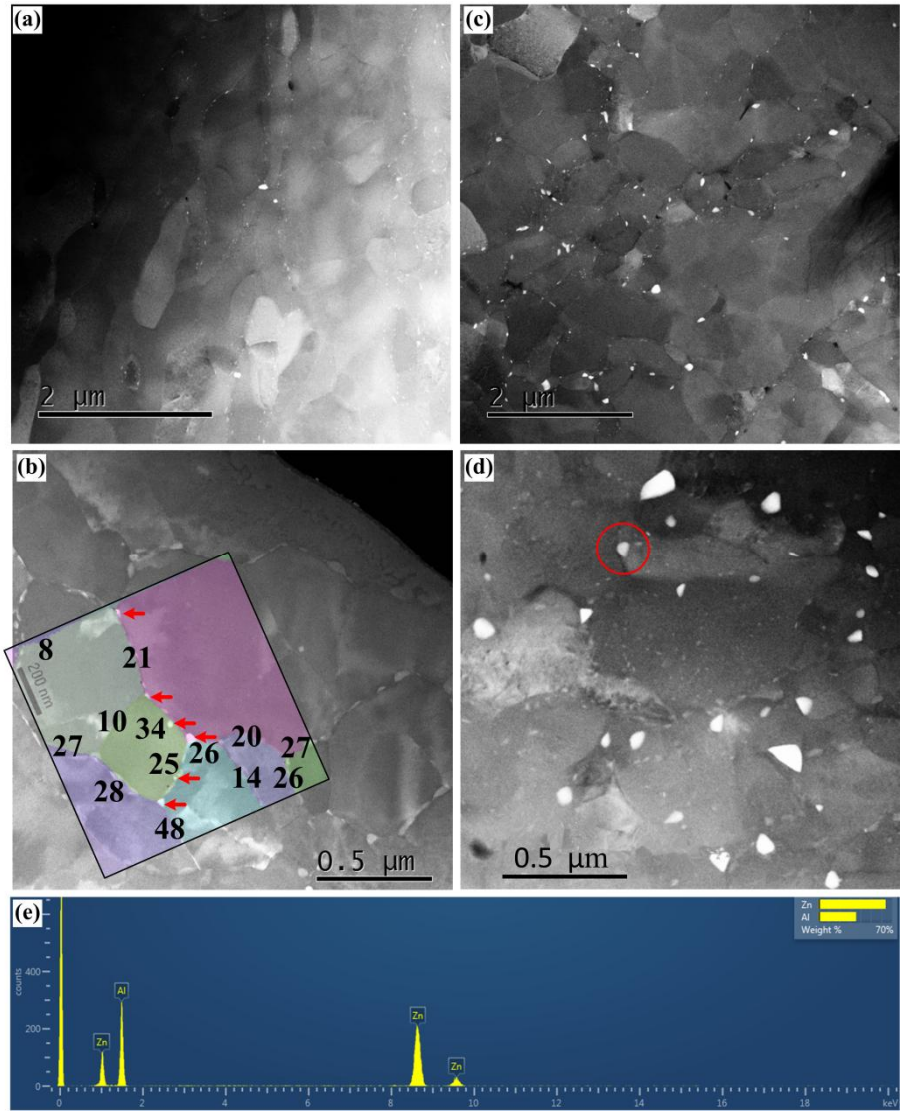

Fig. 7. HAADF (High Angle Annular Dark Field) STEM images of the ECAP processed 5P samples. (a) and (b) Al-8Zn samples, (c) and (d) Al-6Bi-8Zn samples, and (e) is the EDS results of the particle encircled in (d). The inset in (b) is the TEM-SPED map and the misorientation angles of boundaries are given in degree.

3.4. Mechanical properties

3.4.1. Hardness evolution

Fig. 8(a) shows the hardness evolutions of the Al-8Zn and Al-6Bi-8Zn alloys with increasing ECAP passes. In the as-cast state (prior to ECAP processing), the hardness of the Al-6Bi-8Zn alloy is slightly lower than that of the Al-8Zn alloy. During ECAP deformation, the hardness of the Al-6Bi-8Zn alloy increases more rapidly than that of the Al-8Zn alloy. After five passes, the hardness reaches 73 HV, which is much higher than that of the 5P Al-8Bi sample (~40 HV) in a previous work [9]. It means that the addition of Zn is very effective in improving the strength of the Al-Bi based alloys.

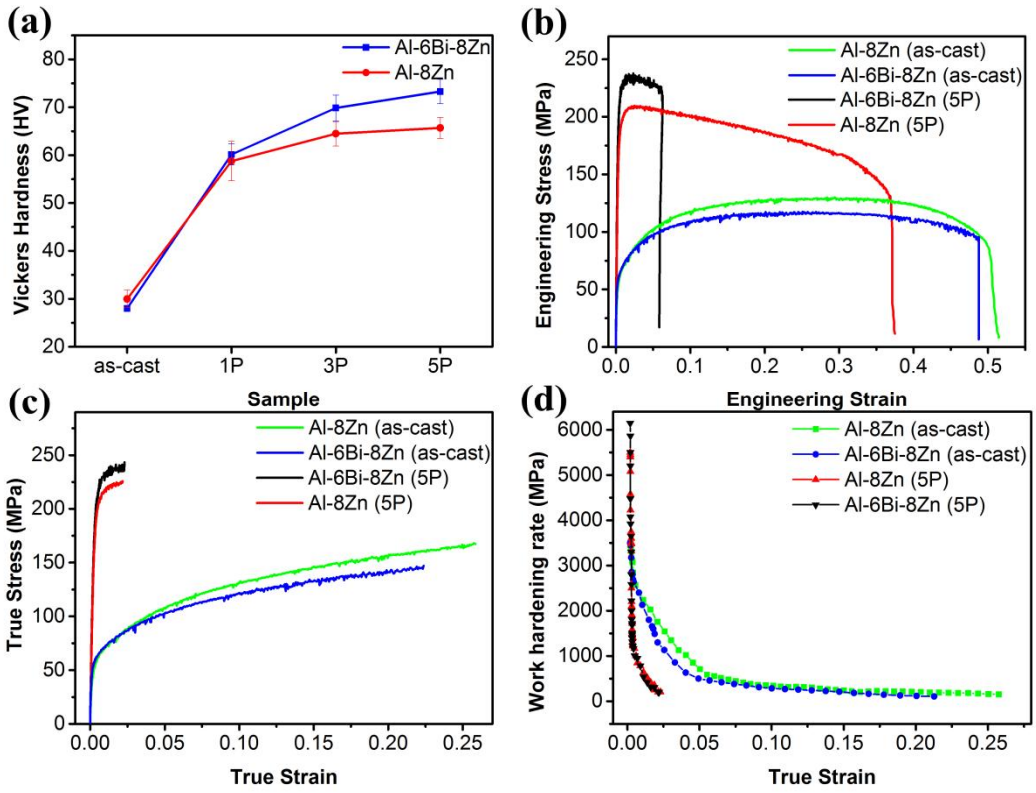

Fig. 8. (a) Hardness evolutions as a function of ECAP passes, (b) engineering stress-strain curves, (c) true stress-strain curves, and (d) work hardening rate curves of the Al-8Zn and Al-6Bi-8Zn alloys.

3.4.2. Tensile properties

Typical engineering stress-strain and true stress-strain curves for the 5P Al-8Zn and 5P Al-6Bi-8Zn samples are shown in Fig. 8(b) and (c), respectively. The tensile properties are summarized in Table 1. The as-cast Al-6Bi-8Zn sample exhibits a slightly lower strength compared to the as-cast Al-8Zn sample. After five passes of ECAP, a substantial improvement in both YS and UTS are achieved in these two alloys.

However, the increase of YS is more significant for the Al-6Bi-8Zn alloy, which is more than three times as that of the as-cast sample. It is interesting to see that both the YS and UTS of the 5P Al-6Bi-8Zn alloy are higher than that of the Al-8Zn alloy.

For both of the two alloys, the improvement of YS after ECAP compared to the as-cast state can be attributed to the grain boundary strengthening and the dislocation strengthening. The introduction of grain refinement through ECAP process leads to a significant strengthening, because grain boundary can impede dislocation movement and dislocation propagation to adjacent grains. The grain boundary strengthening effect can be calculated according to the classical Hall-Petch (HP) relationship $\sigma_y = \sigma_0 + kd^{-1/2}$, where d is the average grain size and k is a material-dependent constant. The average grain sizes of the as-cast samples, the 5P Al-8Zn sample and the 5P Al-6Bi-8Zn sample are 50 μm, 0.9 μm, and 0.5 μm, respectively. Since there is no proper k value for the Al-Zn alloys, it is assumed that it is similar to the Al-3Mg alloy (3.36 at.% Mg) with similar atomic content of additional atoms to Al-8 wt.%Zn, ~105 MPa $\mu m^{1/2}$ [29]. In comparison to the as-cast samples, the grain boundary strengthening $\Delta\sigma_{GB}$ is estimated to be ~96 MPa and ~133 MPa for the 5P Al-8Zn sample and the 5P Al-6Bi-8Zn sample, respectively.

According to classical work hardening theories, the strength contribution from dislocation-dislocation interactions is given by the following relationship: $\Delta\sigma_d = M\alpha Gb\sqrt{\rho}$ [30], where M is the Taylor factor (M = 3), α is a constant measuring the efficiency of dislocation strengthening (α = 3), G is the shear modulus for Al (G = 27 GPa), and b is the Burgers vector (b = 2.86×10^{-10} m). The density of equivalent geometrically necessary dislocations can roughly be estimated by the misorientation gradient according to the equation $\rho \approx \theta/b\delta$ [12] by using the EBSD orientation maps, where θ is the accumulated misorientation angle in radians within a distance δ, and b is the Burgers vector. In this work, based on misorientation gradient measurements of five grains, the average dislocation density is estimated to be ~5×10^{13} m^{-2}. Thus, we can estimate the strength increment from dislocation strengthening $\Delta\sigma_d$ for both of the Al-8Zn and Al-6Bi-8Zn alloys to be ~49 MPa.

The calculated yield strength increases due to grain boundary strengthening and dislocation strengthening are 145 MPa and 182 MPa for the Al-8Zn and Al-6Bi-8Zn alloys, respectively. They are higher than the measured strength increase. This may be attributed to the reduced solid solution level of Zn, resulting in decreased solid solution strengthening.

Table 1. Tensile properties of the Al-8Zn and Al-6Bi-8Zn alloys.

Material	Yield strength (YS) (0.2% offset) [MPa]	Ultimate tensile stress (UTS) [MPa]	Uniform elongation (UE) [%]	Elongation to failure (EF) [%]
Al-8 wt.% Zn (as-cast)	66 ± 2	130 ± 4	26 ± 0.5	51.5 ± 1
Al-8 wt.% Zn (5P)	199 ± 4	221 ± 5	2.2 ± 0.2	37.5 ± 0.6
Al-6 wt.% Bi-8 wt.% Zn (as-cast)	63 ± 3	118 ± 3	22 ± 0.3	48.4 ± 0.8
Al-6 wt.% Bi-8 wt.% Zn (5P)	211 ± 4	238 ± 4	2.3 ± 0.2	6 ± 0.3

The work hardening behavior during tensile test can be seen from Fig. 8(d). The initial work hardening rates of the 5P Al-8Zn and Al-6Bi-8Zn samples are much higher than their as-cast counter parts. However, they decrease quickly with increasing tensile strain, resulting in low uniform elongation values. This is due to the fact that the grains in the 5P samples are nearly supersaturated with dislocations. Thus, the work hardening potential is very limited. Furthermore, it is well known that Zn in solid solution has a strong effect in enhancing the work hardening of Al. Therefore, for the 5P samples, part of Zn in the solid solution has precipitated as particles during ECAP resulting in decrease of the work hardening rate. Although the uniform elongation of the 5P Al-8Zn and 5P Al-6Bi-8Zn samples are almost the same, the value of elongation to failure of the 5P Al-6Bi-8Zn sample is much lower than that of the 5P Al-8Zn sample, which should be related to the presence of a large number of immiscible Bi particles that can act as sources for crack initiation.

3.4.3. Fracture morphology

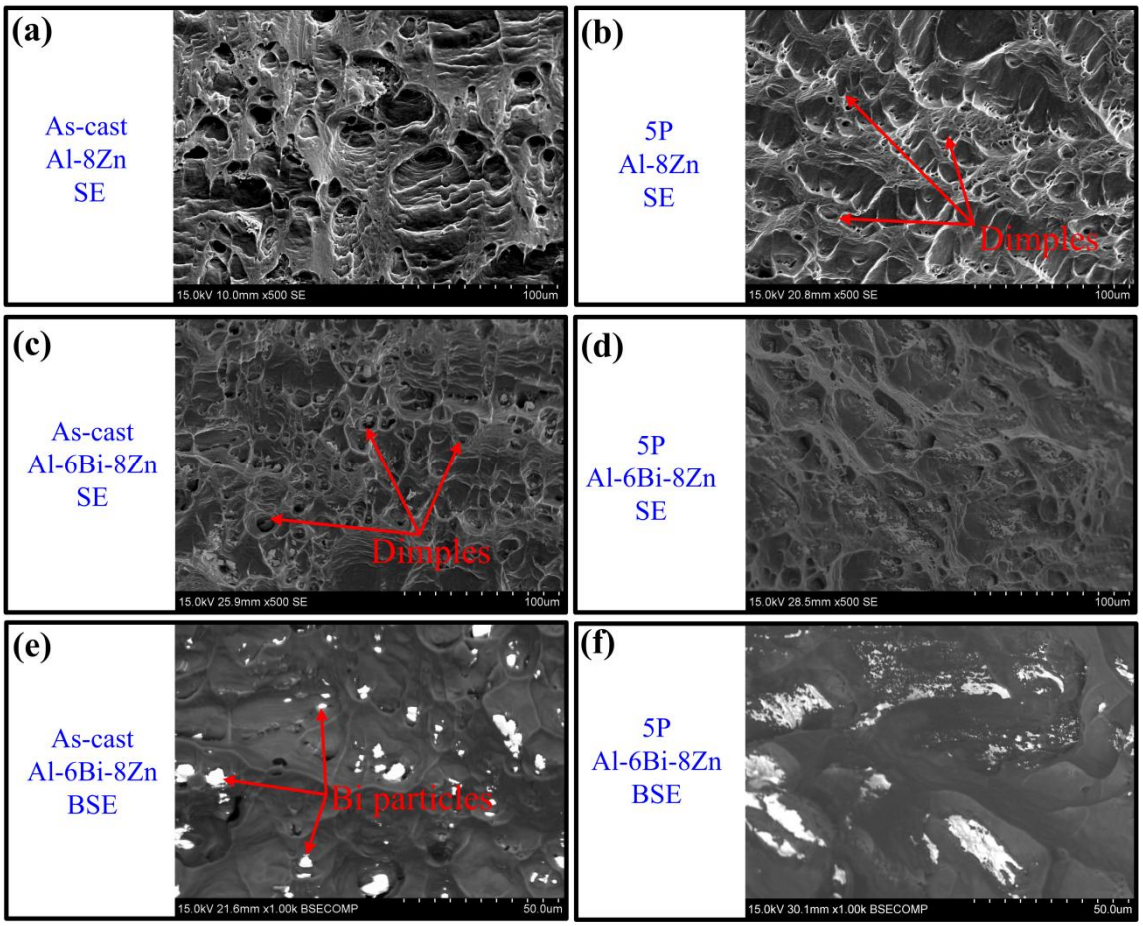

Fig. 9. Fracture morphologies. (a) and (b) SE (secondary electron) images of the as-cast and 5P Al-8Zn samples, respectively; (c) and (d) SE images of the as-cast and 5P Al-6Bi-8Zn samples, respectively; and (e) and (f) BSE images of the as-cast and 5P Al-6Bi-8Zn samples, respectively.

Detailed fracture morphologies of the tensile specimens are shown in Fig. 9. Comparing Fig. 9(a)-(d), we can see that the as-cast samples show a ductile fracture, while the as-deformed samples show a mixture of ductile and brittle fracture. In the 5P Al-8Zn sample (Fig. 9(b)), lots of smaller dimples can be seen, most of which are much shallower than that of the as-cast Al-8Zn sample. However, compared to the 5P Al-8Zn sample, fewer and shallower dimples can be observed in the 5P Al-6Bi-8Zn sample (Fig. 9(d)), which means that the 5P Al-6Bi-8Zn sample is more brittle. As can be seen from Fig. 9(e) and (f), Bi particles are visible in the fracture surfaces of both the as-cast and 5P Al-6Bi-8Zn samples. In contrast to the globular shaped Bi particles distributed at the fracture surface of the as-cast Al-6Bi-8Zn sample, most of the Bi particles show flake shapes in the 5P Al-6Bi-8Zn sample, which is in line with the BSE results in Fig. 2. It implies that the elementary damage event is decohesion of the Bi particle/matrix interfaces,

resulting in poor ductility, which is consistent with the tensile properties. However, flake shaped Bi particles may be good for the lubrication, due to higher surface area of Bi particles.

4. Conclusions

In the present work, we have focused our attention on the microstructural evolution and mechanical properties of an Al-6Bi-8Zn alloy in comparison to an Al-8Zn alloy subjected to ECAP. The following conclusions can be drawn.

(1) UFG microstructures and therefore a substantial increase in strength can be obtained for both the Al-8Zn and Al-6Bi-8Zn alloys.

(2) An addition of 8 wt.% Zn can significantly improve the strength of the Al-Bi alloy for both of the as-cast and the as-deformed state.

(3) The soft Bi particles have a strong influence on enhancing the grain refinement by accelerating the CDRX process, which have a similar effect as hard intermetallic particles.

(4) After ECAP deformation, most of the Bi particles are deformed into flake shapes, which may be good for the lubrication, due to higher surface area of Bi particles.

The results shown in this paper substantiate that for the 5P Al-8wt.% Zn alloy, the sum of the grain boundary strengthening and the dislocation strengthening is larger than softening due to the decomposition of solid solution. Although the results suggest that ECAP can be used as a tool for adjusting the morphology of soft Bi particles, which may be good for lubrication, more detailed experiments and tests have to be further conducted.

Acknowledgements

The authors would like to acknowledge the financial support from Research Council of Norway, under the FRINATEK project ‘BENTMAT’ (Project number 10407002) and China Scholarship Council (201406080011). The authors also appreciate Mr. Pål C. Skaret for his assistance during ECAP experiments and tensile testing.

References

[1] K. Lepper, M. James, J. Chashechkina, D.A. Rigney, Sliding behavior of selected aluminum alloys, Wear 203–204 (1997) 46-56.

[2] L. Ratke, S. Diefenbach, Liquid immiscible alloys, Materials Science and Engineering Reports 15 (1995) 263-347.
[3] T. Wang, F. Cao, Z. Chen, H. Kang, J. Zhu, Y. Fu, T. Xiao, T. Li, Three dimensional microstructures and wear resistance of Al-Bi immiscible alloys with different grain refiners, Science China Technological Sciences 58 (2015) 870-875.
[4] P.L. Schaffer, R.H. Mathiesen, L. Arnberg, L2 droplet interaction with α-Al during solidification of hypermonotectic Al–8 wt.% Bi alloys, Acta Materialia 57 (2009) 2887-2895.
[5] A.P. Silva, J.E. Spinelli, A. Garcia, Microstructural evolution during upward and downward transient directional solidification of hypomonotectic and monotectic Al–Bi alloys, Journal of Alloys and Compounds 480 (2009) 485-493.
[6] A.P. Silva, J.E. Spinelli, A. Garcia, Thermal parameters and microstructure during transient directional solidification of a monotectic Al–Bi alloy, Journal of Alloys and Compounds 475 (2009) 347-351.
[7] A.P. Silva, J.E. Spinelli, N. Mangelinck-Noël, A. Garcia, Microstructural development during transient directional solidification of hypermonotectic Al–Bi alloys, Materials & Design 31 (2010) 4584-4591.
[8] M. Zha, Y. Li, R.H. Mathiesen, H.J. Roven, Dispersion of soft Bi particles and grain refinement of matrix in an Al–Bi alloy by equal channel angular pressing, Journal of Alloys and Compounds 605 (2014) 131-136.
[9] M. Zha, Development and characterization of high solid solution Al-Mg alloys and an immiscible Al-Bi alloy processed by ECAP and annealing (Doctoral Thesis). Faculty of Natural Science and Technology, Norwegian University of Science and Technology, Norway, 2014.
[10] I. Sabirov, M.Y. Murashkin, R.Z. Valiev, Nanostructured aluminium alloys produced by severe plastic deformation: New horizons in development, Materials Science and Engineering: A 560 (2013) 1-24.
[11] H.L. Jia, K. Marthinsen, Y.J. Li, Al-5Cu Alloy Processed by Equal-Channel Angular Pressing, Materials Science Forum 879 (2017) 843-848.
[12] M. Zha, Y. Li, R.H. Mathiesen, R. Bjørge, H.J. Roven, Microstructure evolution and mechanical behavior of a binary Al–7Mg alloy processed by equal-channel angular pressing, Acta Materialia 84 (2015) 42-54.
[13] M. Zha, Y. Li, R.H. Mathiesen, R. Bjørge, H.J. Roven, High ductility bulk nanostructured Al–Mg binary alloy processed by equal channel angular pressing and inter-pass annealing, Scripta Materialia 105 (2015) 22-25.
[14] C.M. Hu, C.M. Lai, P.W. Kao, N.J. Ho, J.C. Huang, Solute-enhanced tensile ductility of ultrafine-grained Al–Zn alloy fabricated by friction stir processing, Scripta Materialia 60 (2009) 639-642.
[15] R. Valiev, M. Murashkin, A. Kilmametov, B. Straumal, N. Chinh, T. Langdon, Unusual super-ductility at room temperature in an ultrafine-grained aluminum alloy, Journal of Materials Science 45 (2010) 4718-4724.
[16] R.Z. Valiev, T.G. Langdon, Principles of equal-channel angular pressing as a processing tool for grain refinement, Progress in Materials Science 51 (2006) 881-981.
[17] A.A. Mazilkin, B.B. Straumal, E. Rabkin, B. Baretzky, S. Enders, S.G. Protasova, O.A. Kogtenkova, R.Z. Valiev, Softening of nanostructured Al–Zn and Al–Mg alloys after severe plastic deformation, Acta Materialia 54 (2006) 3933-3939.
[18] M. Berta, P.J. Apps, P.B. Prangnell, Effect of processing route and second phase particles on grain refinement during equal-channel angular extrusion, Materials Science and Engineering: A 410–411 (2005) 381-385.
[19] H. Jia, R. Bjørge, K. Marthinsen, Y. Li, The deformation and work hardening behaviour of a SPD processed Al-5Cu alloy, Journal of Alloys and Compounds 697 (2017) 239-248.
[20] E.F. Prados, V.L. Sordi, M. Ferrante, The effect of Al_2Cu precipitates on the microstructural evolution, tensile strength, ductility and work-hardening behaviour of a Al–4 wt.% Cu alloy processed by equal-channel angular pressing, Acta Materialia 61 (2013) 115-125.

[21] Z. Liu, X. Chen, X. Han, Y. Gu, The dissolution behavior of θ' phase in Al－Cu binary alloy during equal channel angular pressing and multi-axial compression, Materials Science and Engineering: A 527 (2010) 4300-4305.
[22] J.J. Lewandowski, C. Liu, W.H. Hunt, Effects of matrix microstructure and particle distribution on fracture of an aluminum metal matrix composite, Materials Science and Engineering: A 107 (1989) 241-255.
[23] D.J. Lloyd, Aspects of fracture in particulate reinforced metal matrix composites, Acta Metallurgica et Materialia 39 (1991) 59-71.
[24] S. Ray, Synthesis of cast metal matrix particulate composites, Journal of Materials Science 28 (1993) 5397-5413.
[25] M.A. Muñoz-Morris, I. Gutierrez-Urrutia, D.G. Morris, Effect of equal channel angular pressing on strength and ductility of Al–TiAl composites, Materials Science and Engineering: A 396 (2005) 3-10.
[26] T. Massalski, H. Okamoto, P. Subramanian, L. Kacprzak, Binary alloy phase diagrams, (1990).
[27] Y. Huang, J.D. Robson, P.B. Prangnell, The formation of nanograin structures and accelerated room-temperature theta precipitation in a severely deformed Al–4wt.% Cu alloy, Acta Materialia 58 (2010) 1643-1657.
[28] J.Y. Huang, X.Z. Liao, Y.T. Zhu, F. Zhou, E.J. Lavernia, Grain boundary structure of nanocrystalline Cu processed by cryomilling, Philosophical Magazine 83 (2003) 1407-1419.
[29] M. Furukawa, Z. Horita, M. Nemoto, R.Z. Valiev, T.G. Langdon, Microhardness measurements and the Hall-Petch relationship in an Al-Mg alloy with submicrometer grain size, Acta Materialia 44 (1996) 4619-4629.
[30] H. Mecking, U.F. Kocks, Kinetics of flow and strain-hardening, Acta Metall. 29 (1981) 1865-1875.

Tables.

Table 1. Tensile properties of the Al-8Zn and Al-6Bi-8Zn alloys.

Figure captions.

Fig. 1. (a) and (b) Microstructures of the as-cast Al-6Bi-8Zn alloy, and (c) and (d) microstructures of the as-cast Al-8Zn alloy. (a) and (c) are EBSD orientation imaging map (OIM), (b) and (d) are SEM-BSE micrograph.

Fig. 2. BSE images of the as-deformed Al-6Bi-8Zn samples. (a) and (b) 1 pass, (c) 3 passes, and (d) 5 passes.

Fig. 3. EBSD results of the ECAP processed 1P Al-6Bi-8Zn sample. (a) and (b) Orientation maps, and (c) and (d) corresponding boundary maps of (a) and (b), respectively. (b) is a map with higher magnification of the area encircled by the rectangle in (a). In (a) and (b) black lines depict boundaries with misorientation angles of $15^\circ \leq \Theta < 180^\circ$, and thin grey lines in (b) depict boundaries with misorientation angles of $5^\circ \leq \Theta < 15^\circ$. The inset in (a) is the colour code for the orientation maps. In the boundary maps, green, red and blue lines depict boundaries with misorientation angles of $2^\circ \leq \Theta < 5^\circ$, $5^\circ \leq \Theta < 15^\circ$ and $15^\circ \leq \Theta < 180^\circ$, respectively.

Fig. 4. EBSD results of the ECAP processed 5P Al-6Bi-8Zn and Al-8Zn samples. (a) and (c) Orientation and boundary maps of the 5P Al-6Bi-8Zn sample, respectively. (b) and (d) Orientation and boundary maps of the 5P Al-8Zn sample, respectively. In (a) and (b) black lines depict boundaries with misorientation angles of $15^\circ \leq \Theta < 180^\circ$. In boundary maps green, red and blue lines depict boundaries with misorientation angles of $2^\circ \leq \Theta < 5^\circ$, $5^\circ \leq \Theta < 15^\circ$ and $15^\circ \leq \Theta < 180^\circ$ respectively.

Fig. 5. (a) Evolution of the grain size (with boundary misorientations larger than 5˚) as a function of increasing number of ECAP passes, (b) HAB fraction evolution as a function of increasing number of ECAP passes; (c) and (d) grain size (with boundary misorientations larger than 5˚) distributions of the 5P Al-8Zn and 5P Al-6Bi-8Zn samples.

Fig. 6. High resolution (step size: 0.05 μm) EBSD maps of the as-deformed Al-6Bi-8Zn samples. (a) 1 pass, and (b) 5 passes. In the maps, orientation differences $\Delta\theta \geq 2^\circ$, $\Delta\theta \geq 5^\circ$ and $\Delta\theta \geq 15^\circ$ across boundaries are marked by white, blue and black lines, respectively. Misorientations of selected boundaries are given in degrees.

Fig. 7. HAADF (High Angle Annular Dark Field) STEM images of the ECAP processed 5P samples. (a) and (b) Al-8Zn samples, (c) and (d) Al-6Bi-8Zn samples, and (e) is the EDS results of the particle encircled in (d). The inset in (b) is the TEM-SPED map and the misorientation angles of boundaries are given in degree.

Fig. 8. (a) Hardness evolutions of the Al-8Zn and Al-6Bi-8Zn alloys as a function of ECAP passes, (b) engineering stress-strain curves, (c) true stress-strain curves, and (d) work hardening rate curves.

Fig. 9. Fracture morphologies. (a) and (b) SE (secondary electron) images of the as-cast and 5P Al-8Zn samples, respectively; (c) and (d) SE images of the as-cast and 5P Al-6Bi-8Zn samples, respectively; and (e) and (f) BSE images of the as-cast and 5P Al-6Bi-8Zn samples, respectively.